

See discussions, stats, and author profiles for this publication at: <https://www.researchgate.net/publication/231659551>

# Electronic Structure of the YD Tyrosyl Radical in Photosystem II: A High-Frequency Electron Paramagnetic Resonance Spectroscopic and Density Functional Theoretical Study

ARTICLE *in* THE JOURNAL OF PHYSICAL CHEMISTRY B · AUGUST 1997

Impact Factor: 3.3 · DOI: 10.1021/jp9709518

---

CITATIONS

34

---

READS

13

3 AUTHORS, INCLUDING:



Christian T Farrar

Harvard Medical School

43 PUBLICATIONS 1,990 CITATIONS

SEE PROFILE



Robert G Griffin

Massachusetts Institute of Technology

454 PUBLICATIONS 24,813 CITATIONS

SEE PROFILE

# Electronic Structure of the Y<sub>D</sub> Tyrosyl Radical in Photosystem II: A High-Frequency Electron Paramagnetic Resonance Spectroscopic and Density Functional Theoretical Study

Christian T. Farrar, Gary J. Gerfen,<sup>†</sup> and Robert G. Griffin\*

Department of Chemistry and Francis Bitter Magnet Laboratory, Massachusetts Institute of Technology, Cambridge, Massachusetts 02139

Dee Ann Force and R. David Britt\*

Department of Chemistry, University of California, Davis, California 95616

Received: March 14, 1997; In Final Form: May 28, 1997<sup>⊗</sup>

We report the high-frequency (139.5 GHz) electron paramagnetic resonance (EPR) spectrum of the Y<sub>D</sub> tyrosyl radical of photosystem II. A rhombic powder pattern with principal  $g$  values  $g_1 = 2.007\,82$ ,  $g_2 = 2.004\,50$ , and  $g_3 = 2.002\,32$  is observed. The well-defined turning points and the value of the largest principal  $g$  value are indicative of ordered hydrogen bonding to the tyrosyl phenyl oxygen. Hyperfine structure is resolved on all three turning points. Proton hyperfine couplings obtained from the simulation of the 139.5 GHz EPR spectrum are in good agreement with X-band electron spin echo–electron nuclear double resonance studies. The high-frequency EPR spectrum was acquired under conditions of saturation in which the dispersion signal is detected. Proper replication of the high-frequency EPR spectral features is only achieved in simulations which account for the line shapes characteristic of saturated dispersion signals. Comparison of the Y<sub>D</sub> spectrum with spectra of non-hydrogen bonded tyrosyl radicals indicates that the largest principal  $g$  value ( $g_1$ ), oriented along the C–O bond, is sensitive to hydrogen bonding at the phenyl oxygen. Density functional calculations indicate that the decreased downfield shift in  $g_1$  from the free electron  $g$  value with increasing hydrogen bond strength arises from both a decreased spin density on the phenyl oxygen—5–30% over a range of reasonable hydrogen bond distances (2.0–1.1 Å)—and an increased splitting between ground state and excited state singly occupied molecular orbitals.

## Introduction

Photosystem (PS) II contains two symmetry-related redox active tyrosine residues, Y<sub>D</sub>(D2:Tyr160) and Y<sub>Z</sub>(D1:Tyr161).<sup>1</sup> Y<sub>Z</sub> serves as an electron transfer intermediate between the tetranuclear Mn cluster, where water oxidation occurs, and the photo-oxidized chlorophyll moiety P<sub>680</sub><sup>+</sup>. Additionally, recent models have suggested that the transient Y<sub>Z</sub> radical is directly involved in the water-splitting chemistry, acting to abstract protons<sup>2</sup> or hydrogen atoms<sup>3</sup> from water ligands to the Mn cluster. In contrast, tyrosine Y<sub>D</sub> forms a dark-stable radical Y<sub>D</sub><sup>•</sup>, is bypassed in the light-driven fast electron transfer between the Mn cluster and P<sub>680</sub><sup>+</sup>, and is not essential for photosynthesis. The role of Y<sub>D</sub> is currently unknown; however, the slow growth of the D2-Tyr160Met and D2-Tyr160Phe mutants<sup>4</sup> and the decreased stability of the Mn cluster of the D2-Tyr160Phe mutant to thylakoid isolation and detergent treatment<sup>5</sup> suggest that Y<sub>D</sub> may be involved in protein assembly and stabilization of the Mn cluster. Previous electron spin echo–electron nuclear double resonance (ESE–ENDOR) studies observed hyperfine couplings from <sup>2</sup>H exchangeable protons to both Y<sub>D</sub><sup>•</sup> and Y<sub>Z</sub><sup>•</sup> radicals, which were attributed to protons hydrogen bonded to the phenolic oxygen.<sup>6</sup> The sharply resolved <sup>2</sup>H transitions observed for Y<sub>D</sub><sup>•</sup> are indicative of a structurally defined, well-ordered hydrogen-bonding environment. Assuming a purely dipolar model for the <sup>2</sup>H hyperfine coupling, hydrogen bond distances of 1.67 and 1.87 Å were estimated

for Y<sub>D</sub> from spinach and *Synechocystis* PS II, respectively.<sup>6</sup> The loss of a 3.5 MHz proton ENDOR signal at 9 GHz<sup>4</sup> and the value of  $g_1$  in the 245 GHz EPR spectrum<sup>7</sup> of the D2-His189Gln mutant indicate that His189 either directly or indirectly, via an intervening water molecule, forms this hydrogen bond to Y<sub>D</sub>. More recently, <sup>15</sup>N ESE–ENDOR spectroscopy of Y<sub>D</sub><sup>•</sup> of <sup>15</sup>N-histidine-labeled PS II particles and uniformly <sup>15</sup>N-labeled PS II of the D2-His189Gln mutant has demonstrated that D2-His189 is the direct hydrogen bond donor to Y<sub>D</sub><sup>•</sup>.<sup>8</sup> The well-ordered hydrogen bonding displayed by Y<sub>D</sub><sup>•</sup> suggests a lack of mobility, consistent with its being both oxidized and reduced by P<sub>680</sub><sup>+</sup>/P<sub>680</sub>.

In contrast to Y<sub>D</sub><sup>•</sup>, the broad, poorly resolved <sup>2</sup>H ESE–ENDOR transitions in spectra of the Y<sub>Z</sub><sup>•</sup> radical in Mn-depleted PS II are suggestive of a disordered hydrogen-bonding environment.<sup>6</sup> Analysis of the <sup>2</sup>H electron spin echo envelope modulation (ESEEM) of <sup>2</sup>H-labeled  $\beta$ -methylene hydrogens shows that there is appreciable disorder in the phenoxyl ring orientation in Y<sub>Z</sub><sup>•</sup> of Mn-depleted PS II.<sup>9</sup> The isotropic hyperfine coupling ( $A_{iso}$ ) to the  $\beta$ -methylene protons is proportional to  $\rho_{C1} \cos^2 \theta$ , where  $\rho_{C1}$  is the electron spin density on C<sub>1</sub> (see Figure 1) and  $\theta$  is the angle between the C $\beta$ –H bond and the phenyl ring plane normal. A distribution in this dihedral angle gives rise to a distribution in  $A_{iso}$ . Hydrogen bonding to the phenyl oxygen would provide a barrier to this rotational mobility about the C<sub>1</sub>–C $\beta$  bond. The broad <sup>2</sup>H line widths observed in ESEEM spectra of <sup>2</sup>H $\beta$ -labeled Y<sub>Z</sub><sup>•</sup> therefore suggest rotational mobility about the C<sub>1</sub>–C $\beta$  bond, which may be a result of the disordered hydrogen-bonding environment. The orientational disorder in Y<sub>Z</sub> has been suggested to reflect the high mobility required to switch between defined conformations for reduction and oxida-

\* Authors to whom correspondence should be addressed.

<sup>†</sup> Present address: Department of Physiology and Biophysics, Albert Einstein College of Medicine of Yeshiva University, Bronx, New York 10461.

<sup>⊗</sup> Abstract published in *Advance ACS Abstracts*, July 15, 1997.

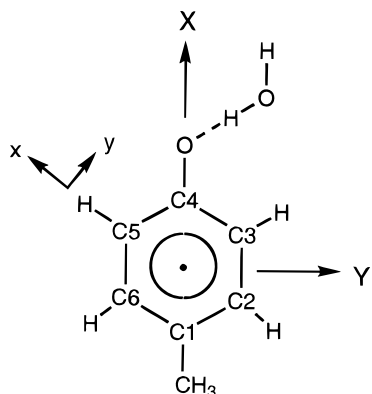


**Figure 1.** Structure of the hydrogen-bonded *p*-methylphenoxyl radical used in the density functional calculations. A water molecule is used to model the hydrogen-bonding group. The molecule-based axis system is denoted in upper case letters, while the principal axes for one of the proton hyperfine interactions is given in lower case letters.

tion by the tetranuclear Mn cluster and P<sub>680</sub><sup>+</sup>, respectively.<sup>10</sup> Relative to Y<sub>D</sub>, the disordered hydrogen bonding and high mobility of Y<sub>Z</sub> would decrease its efficiency if its only role were as a fast electron transfer intermediate. These lines of evidence from ESE–ENDOR, ESEEM, and EPR studies have led to the models in which Y<sub>Z</sub> is directly involved in water oxidation, acting to abstract protons or hydrogen atoms from water bound to the Mn cluster.<sup>2,3</sup> Since the protein environment defines the functional differences between the two PS II tyrosine radicals Y<sub>D</sub> and Y<sub>Z</sub>, it is important to accurately characterize the electronic structures of the two radicals and to understand how these electronic structures are modulated by protein interactions.

Detailed information about the electronic structure and hydrogen-bonding environment of phenoxyl radicals can be gained from high-frequency EPR studies of the electron *g* tensor. Low-frequency EPR studies by Dixon *et al.* of the neutral and cationic (protonated) phenoxyl radicals indicated that the isotropic *g* value (*g*<sub>iso</sub>) is sensitive to the protonation state of the phenyl oxygen.<sup>11</sup> Early low-frequency single-crystal EPR studies of irradiated serine radicals<sup>12</sup> and more recent high-frequency 95 GHz<sup>13</sup> EPR studies of semiquinone radicals suggested that the largest principal *g* value, *g*<sub>1</sub>, is sensitive to solvent polarity and to the protonation or hydrogen-bonding state of the oxygen. Recent high-frequency EPR studies of tyrosyl radicals in PS II<sup>7,14</sup> and ribonucleotide reductase (RNR)<sup>7,15,16</sup> clearly demonstrate the sensitivity of *g*<sub>1</sub> to hydrogen bonding. EPR studies by Gerfen *et al.* at 139.5 GHz<sup>15</sup> of the non-hydrogen bonded tyrosyl radical of *Escherichia coli* RNR obtained principal *g* values of *g*<sub>1</sub> = 2.009 12, *g*<sub>2</sub> = 2.004 57, and *g*<sub>3</sub> = 2.002 25. In contrast, Un *et al.* obtained *g* values of *g*<sub>1</sub> = 2.007 45, *g*<sub>2</sub> = 2.004 22, and *g*<sub>3</sub> = 2.002 11 for the hydrogen-bonded Y<sub>D</sub> radical of PS II from a 245 GHz EPR spectrum.<sup>7,14,17</sup> While *g*<sub>2</sub> and *g*<sub>3</sub> remain effectively unchanged for the two different tyrosyl radicals, *g*<sub>1</sub> displays a noticeable shift to larger *g* value in the absence of a hydrogen bond to the phenyl oxygen. The shift in the principal *g* values from the free electron value (*g*<sub>e</sub> = 2.00 23), given by Δ*g* = *g* – *g*<sub>e</sub>, arises from spin–orbit mixing of the doublet ground state with excited doublet states. The shift in *g*<sub>1</sub> can be shown to be proportional to the spin density on oxygen and inversely proportional to the energy splitting, Δ*E*<sup>\*</sup>, between the ground and excited state singly occupied molecular orbitals (SOMOs).<sup>14,18</sup> A decreased shift in *g*<sub>1</sub> upon hydrogen bonding can therefore be attributed to either a decrease in oxygen spin density, an increase in Δ*E*<sup>\*</sup>, or both. We have performed density functional calculations of model hydrogen-bonded tyrosyl radicals to examine in more detail the

dependence of the electron spin density distribution and MO energies—key parameters in determining the electron *g* values—on the hydrogen bond length. The *p*-methylphenoxyl radical, depicted in Figure 1, is used to model the tyrosyl radical while a water molecule is used to model the hydrogen-bonding group. These calculations are compared with calculations of the non-hydrogen bonded neutral *p*-methylphenoxyl radical found previously to provide accurate electron spin densities and vibrational frequencies.<sup>19</sup> Our density functional calculations indicate both a significant decrease in oxygen spin density and an increased splitting between the ground state and excited state SOMOs with decreasing hydrogen bond length.

## Materials and Methods

**Photosystem II Sample Preparation.** Oxygen-evolving PS II-enriched membranes were prepared from market spinach by the method of Berthold *et al.*<sup>20</sup> and Ford and Evans<sup>21</sup> with minor modifications. Samples (about 1.0 μL) at 18 mg of chlorophyll per mL in 400 mM sucrose/50 mM MES–NaOH, pH 6.0/15 mM NaCl/5 mM CaCl<sub>2</sub>/5 mM MgCl<sub>2</sub>, were packed into 0.4 mm (i.d.) quartz capillary tubes and dark-adapted on ice for 45 min before freezing on dry ice and subsequent storage at 77 K. O<sub>2</sub> evolution rates were 500 μmol of O<sub>2</sub>/mg of chlorophyll/h. Chlorophyll determination was done according to Arnon.<sup>22</sup>

**High-Frequency EPR Spectroscopy.** The PS II EPR spectrum was acquired in the continuous wave (CW) saturated dispersion mode using a 139.5 GHz heterodyne spectrometer with phase-sensitive detection designed and fabricated in this laboratory.<sup>23</sup> Typical saturating conditions were as follows: microwave power at the sample was ~20 μW corresponding to a *B*<sub>1</sub> field of ~0.1 G; temperature equal to 16 K; and modulation amplitude and frequency equal to 1.0 G and 400 Hz, respectively. The external magnetic field was swept over a 400 G range at 2.0 G/s. The 18 μs *T*<sub>1</sub> used to simulate the α,γ-bisdiphenylene-β-phenylallyl (BDPA) spectra of Figure 2 was determined from a 139.5 GHz saturation recovery electron spin echo experiment. No spin echoes were observed for Y<sub>D</sub>, preventing an independent experimental determination of *T*<sub>1</sub>. A reasonable value for the *T*<sub>1</sub> of Y<sub>D</sub> was obtained from the best fit simulation of the experimental line shape. Saturation and adiabatic passage effects in high-frequency EPR spectroscopy are discussed more extensively in the Results and Discussion section. The sample tube was inserted into a cylindrical TE<sub>011</sub> resonator under liquid nitrogen, and the EPR probe was loaded into a precooled cryostat as previously described.<sup>24</sup> A steady flow of cold helium gas over the cavity provided sample cooling during the experiments.

**Spectral Simulations.** All EPR spectra were simulated, as previously described,<sup>24</sup> with the following adjustable parameters: the three principal values of the *g* tensor; the three principal values of each hyperfine interaction matrix; the orientation of the principal axes of each hyperfine matrix within the Zeeman interaction principal axis system; the modulation frequency (ω<sub>m</sub>) and amplitude (*B*<sub>m</sub>); the electron spin–lattice relaxation time (*T*<sub>1</sub>); and the microwave field strength (*B*<sub>1</sub>). The resonant fields (*B*<sub>res</sub>) were determined using eq 1, in which θ is

$$B_{\text{res}}(\theta, \phi, m_1^1, \dots, m_1^n) = \frac{\hbar \omega_e}{g(\theta, \phi) \beta} - \sum_{i=1}^n m_1^i A_i(\theta, \phi) \quad (1)$$

the polar angle and φ is the azimuthal angle that together specify the orientation of the external magnetic field *B*<sub>0</sub> in the Zeeman principal axis system, ħ is Planck's constant, ω<sub>e</sub> is the microwave frequency, *g*(θ, φ) is the orientationally dependent *g* value, β is the Bohr magneton, and *A*<sub>*i*</sub>(θ, φ) is the orienta-

tionally dependent hyperfine coupling to the  $i$ th nucleus. In the simulation of orientationally disordered samples 180 polar angles were sampled at equal intervals over the range  $0-\pi$ . At each polar angle, between one and 360 azimuthal angles (the number being nearly equal to 360 times the sine of the polar angle) were sampled at equal intervals over the range  $0-2\pi$ . At each orientation the resonant fields were calculated, and the resulting distribution of resonant fields were convolved with the saturated dispersion line shape (see Results and Discussion). An orientational dependent broadening function was incorporated into the saturated dispersion line shape by varying  $\Delta B$  (see eq 2) along the different  $g$  principal axes. The simulations were then pseudomodulated<sup>25</sup> in a manner identical to the experimental data in order to display the spectra in a more conventional "derivative" mode.

**Density Functional Calculations.** Theoretical calculations were performed with the Gaussian94 suite of programs.<sup>26</sup> Slater's local spin density exchange function<sup>27</sup> and the local spin density correlation functional of Vosko, Wilk, and Nusair<sup>28</sup> (SVWN) were employed with the 6-31G(d)<sup>29,30</sup> basis set. The SVWN/6-31G(d) basis set has previously been found to give good agreement with experimental spin densities, vibrational frequencies, and structures for the neutral and cation indolyl radicals<sup>31</sup>—models for tryptophan—as well as the neutral phenoxyl and tyrosyl radicals<sup>32</sup> and the tyrosyl cation radical.<sup>33</sup> The  $p$ -methylphenoxyl radical serves as a good model for the tyrosyl radical—the calculated spin densities differ by less than 0.03 between the two radicals, indicating that the unpaired electron of tyrosine resides entirely on the phenoxyl side chain.<sup>32</sup> The optimized geometry for the neutral tyrosyl radical was taken from a CASSCF<sup>34,35</sup>/6-311G(2d,p) calculation.<sup>19</sup> The hydrogen bond angle for the hydrogen-bonded radical was optimized at the 6-31G(d) basis set level; a hydrogen bond angle of  $105.5^\circ$  was obtained. Calculations were also performed as a function of the hydrogen bond angle. A variation of this bond angle by as much as  $+35^\circ$  resulted in less than a 3% decrease in the oxygen spin density. The expectation value of  $\langle S^2 \rangle = S(S+1) = 0.75$  for all calculations indicates that the calculated ground state is a good representation of the doublet state of the  $S = 1/2$  radical.

## Results and Discussion

**High-Frequency EPR Spectrum of  $Y_D$ .** The small  $g$ -anisotropy of the PS II  $Y_D$  tyrosyl radical is easily resolved in the 139.5 GHz pseudomodulated, saturated dispersion EPR spectrum of Figure 2A, yielding principal  $g$  values of  $g_1 = 2.007\ 82$ ,  $g_2 = 2.004\ 50$ , and  $g_3 = 2.002\ 32$ . The well-defined  $g_1$  edge of the  $Y_D$  powder pattern is an indication of a defined hydrogen-bonding environment for  $Y_D$ ; a distribution in hydrogen bond strengths would give rise to a distribution in  $g_1$ . Such a broadening of the  $g_1$  edge was observed in the 245 GHz spectrum of  $Y_Z$  of Mn-depleted PS II, which is believed to exist in a disordered hydrogen-bonding environment.<sup>14</sup> In contrast to previous high-field studies at 245 GHz,<sup>7,14</sup> we observe hyperfine structure on all three turning points of the  $Y_D$  spectrum (Figure 2A). Resolution of the hyperfine structure on the different edges allows for the correlation of the  $g$  and hyperfine tensor orientations. Traces B and C of Figure 2 are the simulated fits of the experimental high-frequency spectrum for saturated dispersion and absorption modes, respectively, which were performed for coupling to three protons: the 3,5-ring protons and the more strongly coupled  $\beta$ -proton of tyrosine. Good fits of the experimental spectrum were only obtained for simulations which incorporated the saturated dispersion line shape discussed below. The hyperfine couplings (see Table 1)

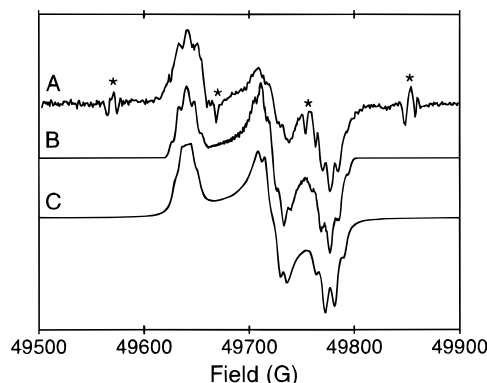


**Figure 2.** (A) 139.5 GHz pseudomodulated saturated dispersion (modulation-detected) EPR spectrum of the  $Y_D$  tyrosyl radical in dark-adapted photosystem II acquired at 16 K along with simulations incorporating (B) a pseudomodulated saturated dispersion line shape and (C) a pseudomodulated absorption line shape. The hyperfine couplings and electron  $g$  values used in the simulations are given in Tables 1 and 2, respectively. The saturation parameters used in the saturated dispersion simulation are:  $\nu_m = 400$  Hz,  $B_m = 1.0$  G,  $B_1 = 0.1$  G,  $T_1 = 75$   $\mu$ s. The peaks marked with an asterisk (\*) arise from trace free  $Mn^{2+}$  present in the sample.

**TABLE 1: Principal Hyperfine Values ( $A$ , MHz) and Orientations<sup>a</sup> (deg) Used in Simulations of the High-Frequency (139.5 GHz) EPR and Low-Frequency (14.8 GHz) ESE-ENDOR<sup>2</sup> Spectra of  $Y_D$**

proton position	$A_x$	$A_y$	$A_z$	$\alpha$	$\beta$	$\gamma$	ref
2,6	3.7	3.7	7.0				2
5 or 3	14.8	18.8	23.0	0	0	-30	this work
	12.3	18.8	23.0				2
3 or 5	14.8	20.3	23.0	0	0	30	this work
	12.3	20.3	23.0				2
$\beta_1$	27.0	27.0	30.5	47	0	0	2, this work
$\beta_2$	3.7	3.7	9.2	73	0	0	2

<sup>a</sup>  $\alpha$ ,  $\beta$ , and  $\gamma$  are the Euler angles that relate the principal axes of the hyperfine interaction ( $x, y, z$ ) to the principal axes of the electron Zeeman interaction ( $X, Y, Z$ ).  $\alpha$  and  $\beta$  are the ordinary polar coordinates of the  $z$  axis in the  $XYZ$  coordinate system. The Euler angles define a rotation of the  $z$  axis by an angle  $\alpha$  about the  $X$  axis, followed by a rotation of the  $z$  axis by an angle  $\beta$  about the  $Z$  axis, and finally a rotation of the  $xy$  plane by an angle  $\gamma$  about the  $z$  axis.

obtained from the simulation are in good agreement with those obtained for Mn-depleted PS II samples from a previous  $^1H$  ESE-ENDOR study by Gilchrist *et al.*,<sup>2</sup> a  $^2H$  ESEEM study by Warnke *et al.*,<sup>36</sup> as well as an earlier CW ENDOR study by Rigby *et al.*<sup>37</sup> While the number of parameters used in the fits of the low-field ENDOR and high-field EPR data is quite large, the good agreement between the two simulations provides credence for the uniqueness of the couplings extracted and also indicates that removal of the Mn cluster in the ENDOR studies does not alter the electronic structure or the observed hyperfine couplings of  $Y_D$ .

**Saturated Dispersion EPR Spectra.** The high-frequency spectrum of  $Y_D$  was acquired under conditions which maximized the saturated first harmonic (modulation-detected) dispersion signal.<sup>38-40</sup> Modulation-detected saturated dispersion signals have an unconventional appearance that under certain conditions appears similar to that of direct-detected absorption signals, but with increased line widths. The theory of saturated dispersion line shapes has been treated extensively by Ammerlaan and van der Weil.<sup>41</sup> The analytical expression for the component of the saturated dispersion signal in phase with the magnetic field modulation, used in the simulation of the EPR spectrum, is given by eq 2<sup>41</sup>

$$\chi_0'(b) = \frac{1}{8}(2\pi)^{1/2} \chi_0 b_0 \frac{b_m}{b_1} \exp(-b^2/2) \left( \frac{C_2}{1 + \omega_m^2 T_1^2} - 2C_1 + C_2 + \frac{1}{2} \left[ \frac{2C_1 - C_2}{1 + \omega_m^2 T_1^2} + 4C_1 - C_2 - \frac{2}{b_1} \left( \frac{2}{\pi} \right)^{1/2} \right] b_1^2 b^2 \right) \quad (2)$$

where  $B_0$  = static field,  $B_1$  = microwave field,  $B_m$  = modulation field,  $B'$  = field scan rate,  $\Delta B$  = line width,  $b_0 = B_0/\Delta B$ ,  $b_1 = B_1/\Delta B$ ,  $b_m = B_m/\Delta B$ ,  $b = (B' t)/\Delta B$ ,  $T_1$  = spin–lattice relaxation time,  $\mu = T_1 (B'/B_1)$ , and

$$C_n(b_1) = \frac{2^{2n-2} \{(n-1)!\}^2}{\pi(2n-2)!} \int_{-\infty}^{+\infty} dx \frac{1}{(1+x^2)^n} \exp\left(\frac{-b_1^2 x^2}{2}\right)$$

$$C_1(b_1) = \operatorname{erfc}(b_1/\sqrt{2}) \exp(b_1^2/2)$$

$$C_2(b_1) = b_1 (2/\pi)^{1/2} + (1 - b_1^2) C_1$$

Equation 2 was derived from the solution to Bloch's equations obtained by Portis<sup>40</sup> and is valid under conditions of (1) adiabatic passage,  $B' \ll \gamma B_1^2$  and  $\omega_m B_m \ll \gamma B_1^2$ , and (2) saturation of the resonance,  $\gamma B_1 T_1 \gg 1$ . The solution contains integrands which are approximated, as in the derivation of Ammerlaan and van der Weil,<sup>41</sup> by a power series expansion in  $b_m/b_1$  to obtain the analytic expression of eq 2. This expansion is valid only if the series converges, a condition satisfied for  $b_m \ll b_1$ . Equation 2 was derived by retaining only the leading term in this expansion. A final approximation of a slow linear scan,  $\mu = T_1 (B'/B_1) \ll \omega_m T_1$  and  $\mu \ll 1$ , is required in order to evaluate certain integrals in the differential eqs by repeated integration by parts. All the above conditions are satisfied in our experiments with the exception of  $b_m \ll b_1$ ;  $b_m$  is typically 1–10 times greater than  $b_1$  for our experimental conditions (see Materials and Methods). However,  $b_m/b_1 \ll 1$  is a sufficient but not necessary condition for convergence of the power series expansion. In order to experimentally verify the validity of eq 2 for  $b_m > b_1$ , we undertook a study of a sample of 2 wt % BDPA doped into polystyrene (2.0% BDPA/PS)—a system for which relaxation times have been independently determined using high-frequency pulsed EPR.<sup>23</sup> In Figure 3 we display CW EPR spectra of 2.0% BDPA/PS as a function of the modulation frequency,  $\omega_m$ . Depending on the values of  $\omega_m T_1$  and  $b_1$ , eq 2 describes a variety of resonance line shapes as discussed by Ammerlaan and van der Weil.<sup>41</sup> Using the independently determined value of  $T_{1e}$  for 2% BDPA/PS and known values of  $\omega_m$ ,  $B_m$ , and  $B_1$ , we find that the experimental BDPA/PS line shapes are all accurately replicated by the simulations. The fact that the simulations, with no adjustable parameters, accurately reproduce the experimental line shapes indicates that eq 2 is valid under our experimental conditions.

Pseudomodulation of the Y<sub>D</sub> PS II saturated dispersion spectrum (Figure 2A), following the methods developed by Hyde *et al.*,<sup>25</sup> is performed to provide the more conventional “derivative” representation of the experimental spectrum. A comparison of traces B and C of Figure 2, the saturated dispersion and absorption line shape simulated spectra, respectively, indicates the necessity of accounting for the saturation conditions to faithfully replicate the experimental spectral features. Both simulations employ the same hyperfine and  $g$  tensor parameters (see Tables 1 and 2), yet the hyperfine structure of the simulated absorption spectrum differs markedly from both the saturated dispersion simulation and the experimental spectrum; the high-field minimum in the saturated dispersion simulation of Figure 2B, for example, corresponds

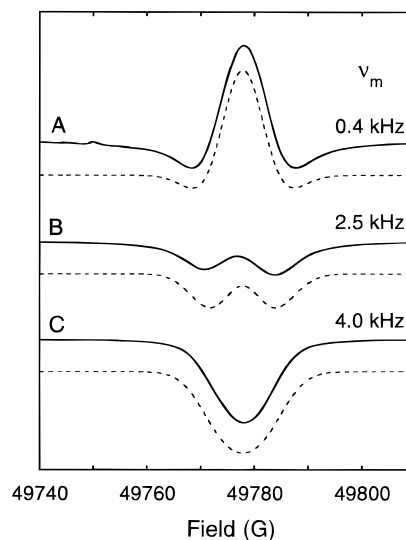


**Figure 3.** Experimental (solid traces) and simulated (dashed traces) 139.5 GHz CW EPR spectra of 2.0% BDPA/PS acquired with modulation frequencies,  $\nu_m$ , of (A) 400 Hz, (B) 2.5 kHz, and (C) 4.0 kHz. The parameters used in the saturated dispersion simulations are  $g_1 = g_2 = 2.00236$ ,  $g_3 = 2.00220$ ,  $B_m = 1.0$  G,  $B_1 = 0.4$  G,  $T_1 = 18.0$   $\mu$ s, and a 9.0 G line broadening.

**TABLE 2: Principal  $g$  Values and Hydrogen Bond (HB) Distances for Various Tyrosyl Radicals**

	HB (Å)	$g_1$	$g_2$	$g_3$	ref
<i>E. coli</i> RNR	none	2.009 12	2.004 57	2.002 25	15
<i>S. typhimurium</i> RNR		2.008 97	2.004 37	2.002 17	56
PS II (Y <sub>D</sub> )	1.7–1.9	2.007 82	2.004 50	2.002 32	this work
mouse RNR		2.0076	2.0043	2.0022	16
Tyr single crystal	1.6	2.0067	2.0045	2.0023	51

to a local maximum in the absorption simulation of Figure 2C. The negative side lobes evident in the BDPA/PS spectra of Figure 3B suggest that under these conditions of saturation, interference between overlapping peaks and troughs of different hyperfine lines could give rise to the distorted hyperfine structure observed in the saturated dispersion spectrum of Y<sub>D</sub> in Figure 2B. A line shape reminiscent of an unmodulated absorption spectrum may be obtained in the dispersion spectrum as the power and/or modulation frequency is increased, as observed with the 2% BDPA/PS sample in Figure 3C. However, an increase in power also led to increased line widths, which prevented the resolution of the hyperfine structure of the Y<sub>D</sub> dispersion signal. Moreover, increasing the microwave power (5–15 dB) or decreasing the temperature (31–10 K) also resulted in an attenuation of the center of the Y<sub>D</sub> EPR spectrum with respect to the shoulders, suggesting the onset of saturation of the dispersion signal. The center of the experimental dispersion EPR powder pattern in Figure 2A (acquired at 16 K) is also attenuated with respect to the center of the simulated spectrum, which again suggests saturation of the dispersion signal.

**Implications of  $g$  Value Shifts for Electronic Structure and Hydrogen Bonding.** Low-frequency EPR studies by Dixon *et al.* of the neutral and cationic (protonated) phenoxyl radicals indicated that the isotropic  $g$  value ( $g_{iso}$ ) is sensitive to hydrogen bonding to the phenyl oxygen;  $g_{iso}$  values of 2.0044 and 2.0033 were observed for the neutral and cationic radicals, respectively.<sup>11</sup> Other low-frequency EPR studies of phenoxyl radicals have postulated a direct proportionality between the oxygen spin density ( $\rho_O$ ) and  $g_{iso}$ .<sup>42–44</sup> As noted in previous high-frequency EPR studies, a comparison of the principal  $g$

**TABLE 3: Total Atomic Mulliken Spin Densities of the Neutral and Hydrogen-Bonded *p*-Methylphenoxyl Radicals as a Function of Hydrogen Bond Length (Å)<sup>a</sup>**

H bond	1.1	1.3	1.5	1.6	1.7	1.8	2.0	none
$\rho_O$	0.248	0.274	0.294	0.301	0.306	0.309	0.314	0.330
$\rho_{C_1}$	0.272	0.298	0.314	0.317	0.322	0.323	0.323	0.321
$\rho_{C_2}$	-0.034	-0.043	-0.050	-0.051	-0.052	-0.053	-0.054	-0.055
$\rho_{C_3}$	0.182	0.202	0.215	0.219	0.221	0.223	0.224	0.230
$\rho_{C_4}$	0.033	0.032	0.028	0.026	0.024	0.021	0.016	-0.006
$\rho_{C_5}$	0.178	0.198	0.212	0.216	0.219	0.221	0.224	0.230
$\rho_{C_6}$	-0.042	-0.045	-0.048	-0.048	-0.050	-0.051	-0.052	-0.057
$\rho_{C\beta}$	-0.009	-0.010	-0.011	-0.011	-0.012	-0.012	-0.012	-0.013
$\rho_{O(H_2O)}$	0.164	0.082	0.029	0.013	0.005	0.001	0.000	

<sup>a</sup> H<sub>2</sub>O is used to model the hydrogen-bonding group. All calculations employed the Gaussian94 suite of programs and the SVWN/6-31G(d) basis set.

values from hydrogen-bonded and non-hydrogen bonded tyrosyl radicals indicates that the largest  $g$  value ( $g_1$ ), oriented along the C–O bond, is a sensitive monitor of solvent polarity and hydrogen bonding at the phenyl oxygen.<sup>7,13–16</sup> The three principal  $g$  values for a variety of hydrogen-bonded tyrosyl radicals are tabulated in Table 2. The smallest  $g_1$  value is observed in EPR studies of the strongly hydrogen-bonded tyrosine hydrochloride radical;<sup>51</sup> a 1.6 Å proton-oxygen bond is observed in the neutron diffraction study of diamagnetic Tyr•HCl by Frey *et al.*<sup>45</sup> In contrast, the tyrosyl radical of *E. coli* RNR has no hydrogen bond<sup>46</sup> and exhibits the largest  $g_1$  value.<sup>7,15</sup> The high-frequency EPR spectrum of mouse RNR has recently been recorded, and the value of  $g_1$  indicates a hydrogen bond similar to that of Y<sub>D</sub> in PS II from *Synechocystis*.<sup>16</sup>

The shift in  $g_1$  from the free electron  $g$  value,  $g_e$ , arises due to spin–orbit coupling of the ground state to excited states with non-zero orbital angular momentum and has been treated extensively by Stone.<sup>18,47,48</sup> In the absence of spin–orbit coupling, the ground state wave function is non-degenerate, due to the low  $C_s$  symmetry of the tyrosyl radical, and orbital angular momentum is quenched, resulting in an isotropic electron Zeeman interaction. The shifts in the  $g$  values due to spin–orbit coupling, expressed in the molecular frame, are approximated by eq 3

$$\Delta g_{\alpha\beta} = \sum_{i \neq j} \sum_k \langle \psi^{(j)} | L_{\alpha}^{(k)} | \psi^{(i)} \rangle \sum_k \frac{\zeta^{(k)}}{(\epsilon_i - \epsilon_j)} \langle \psi^{(i)} | L_{\beta}^{(k)} | \psi^{(j)} \rangle \quad (3)$$

where  $i$  indexes MOs,  $j$  is the index of the SOMO,  $k$  and  $k'$  index atoms,  $\zeta^{(k)}$  is the one-electron atomic spin–orbit coupling constant for the  $k$ th atom,  $\epsilon_i$  is the eigenvalue of the  $i$ th MO,  $L$  is the orbital angular momentum operator, and  $\alpha(\beta)$  is the molecular axis  $X$ ,  $Y$ , or  $Z$ . For tyrosine, the out-of-plane component of  $g$  ( $g_{zz}$ ) is approximately equal to the free electron value ( $g_e$ ) while the in-plane components ( $g_{xx}$ ,  $g_{yy}$ ) are shifted to higher  $g$  values. The  $g_1$  principal axis for the tyrosyl radical is to a good approximation aligned along the  $X$  molecular axis (see Figure 1). For illustrative purposes, eq 3 can be used to approximate the shift in  $g_1$  by considering only one-center contributions from the oxygen

$$\Delta g_1 = \Delta g_{xx} \approx \zeta_O \frac{\rho_O^{\pi} \rho_O^*}{\Delta E^*} \quad (4)$$

where  $\zeta_O$  represents the oxygen spin–orbit coupling constant ( $\zeta_O = 147 \text{ cm}^{-1}$ ),  $\rho_O^{\pi}$  represents the ground state SOMO electron spin density on oxygen,  $\rho_O^*$  represents the spin density in an excited state SOMO corresponding to a nonbonding MO center on oxygen, and  $\Delta E^*$  is the energy splitting between the ground and excited state SOMOs.<sup>14,18</sup>

To examine in more detail the connection between hydrogen bonding and the electronic structure, and hence the electron  $g$  shifts, we have performed density functional calculations on a model tyrosyl radical, *p*-methylphenoxyl (see Figure 1), as a function of hydrogen bond length. Within the perturbative treatment which leads to eqs 3 and 4, it is evident that the shift in  $g_1$  can derive from two sources—a change in the energy splitting  $\Delta E$  or a redistribution of spin density. In Table 3 we present the results of our density functional calculations of the spin density distribution in the *p*-methylphenoxyl neutral and hydrogen-bonded radicals in which a water molecule models the hydrogen-bonding group. The hydrogen bond distance was varied over a reasonable Y<sub>D</sub> hydrogen bond length range of 1.1–2.0 Å. The spin densities are compared with those calculated for the neutral *p*-methylphenoxyl radical by us and Qin *et al.*<sup>19,32</sup> The neutral, non-hydrogen bonded radical displays even/odd alternate spin density with large (positive) spin density on C<sub>1</sub>, C<sub>3</sub>, and C<sub>5</sub>, and small (negative) spin density on C<sub>2</sub>, C<sub>4</sub>, and C<sub>6</sub>. Upon hydrogen bonding, a 5–30% decrease in oxygen spin density is observed as the hydrogen bond distance is decreased from 2.0 to 1.1 Å. The large spin densities on C<sub>1</sub>, C<sub>3</sub>, and C<sub>5</sub> decrease, while the small spin densities on C<sub>2</sub>, C<sub>4</sub>, and C<sub>6</sub> increase, with decreasing hydrogen bond length. At 1.1 Å a noticeable spin density is also apparent on the oxygen of the hydrogen-bonded water. An optimized hydrogen bond angle (C4–O–H–) of 105.5° was used for these calculations. The bond angle in a protein may deviate from this optimized geometry; therefore, calculations were performed as a function of the hydrogen bond angle. Un *et al.* estimated a 140° hydrogen bond angle for Y<sub>D</sub> in photosystem II.<sup>7</sup> In our calculations the oxygen spin density calculated for a 140° hydrogen bond angle decreased by less than 3% from that of the optimized geometry.

Qualitatively, our studies demonstrate the same trend in electron spin density as a function of hydrogen bonding as was observed in intermediate neglect of differential overlap (INDO) calculations by Feher *et al.* of ubisemiquinone radicals in which hydrogen bonding (1.5 Å) to the two carbonyl oxygens of the quinone results in a decreased spin density on the oxygens and an increased density on the adjacent ring carbons.<sup>49</sup> Similarly, INDO calculations by Burghaus *et al.* of semiquinone radicals indicated an increased polarity of the C–O fragment upon hydrogen bonding, which decreases the value of  $\rho_O^{\pi}$  in favor of  $\rho_{C_4}^{\pi}$ .<sup>13</sup> In our density functional calculations we observe a 10% decrease in the oxygen spin density (from 0.33 to 0.30) for a 1.7 Å hydrogen bond. A recent density functional study by Himo *et al.* of model tyrosyl radicals where the hydrogen-bonding group was modeled by formic acid reported a 15% decrease in oxygen spin density (from 0.37 to 0.32) in the presence of a ~1.6 Å hydrogen bond.<sup>50</sup> Theoretical modified neglect of differential overlap (MNDO) calculations by

**TABLE 4: Experimental Electron Spin Density ( $\rho$ ) Distribution and Hydrogen Bond Length (HB) for Various Tyrosyl Radicals<sup>a</sup>**

radical	HB (Å)	$\rho_O$	$\rho_{C_1}$	$\rho_{C_3}$	$\rho_{C_5}$	ref
spinach Y <sub>D</sub>	1.7 <sup>6</sup>	0.22	0.4	0.26	0.27	37
<i>C. reinhardtii</i> Y <sub>D</sub>		0.22	0.4	0.26	0.27	37
<i>P. laminosum</i> Y <sub>D</sub>		0.22	0.4	0.26	0.27	37
<i>Synechocystis</i> Y <sub>D</sub>	1.7 <sup>7</sup> , 1.9 <sup>6</sup>	0.26	0.37	0.24	0.24	36
<i>Synechocystis</i> Y <sub>Z</sub>		0.26	0.37	0.26	0.26	9
Tyr (aqueous glass)		0.26	0.34	0.24	0.24	53, 57
<i>E. coli</i> RNR	none <sup>46</sup>	0.29	0.38	0.25	0.25	53
Tyr•HCl (crystal)	1.6 <sup>45</sup>	0.30	0.32	0.24	0.24	51
Mouse RNR		0.34	0.33	0.25	0.25	58
<i>S. typhimurium</i> RNR		0.25–0.49	0.16–0.40	0.28	0.28	56

<sup>a</sup> All the experimentally determined spin densities are calculated with the McConnell relation from ENDOR- and EPR-measured hyperfine couplings.

Un *et al.* of the *p*-methylphenoxyl radical observed a 10% decrease in oxygen spin density (from 0.24 to 0.22) with a 1.7 Å hydrogen bond to the phenyl oxygen, where acetic acid was used to model the hydrogen-bonding group.<sup>7</sup> Despite some differences in the magnitude of the spin densities, all of the above theoretical studies observed a significant decrease in oxygen spin density of 10–15% for weak hydrogen-bonding regardless of the structural model, hydrogen bonding group, or basis set used.

In our density functional calculations of the *p*-methylphenoxyl radical, the MO energies were also observed to change upon hydrogen bonding and will influence the electron *g* values. The calculations were performed using the optimized 105.5° C<sub>4</sub>–O–H bond angle. The splitting between the ground state highest occupied molecular orbital (HOMO) and the nearest unoccupied MO is taken as an approximation of the energy splitting between the ground state SOMO and the first excited state SOMO in which an  $\alpha$  or  $\beta$  electron is promoted from the occupied to virtual MO. The splitting between the occupied and virtual  $\alpha$  MOs increased upon hydrogen bonding. Previous INDO calculations of semiquinone radicals by Burghaus<sup>13</sup> and MNDO calculations of the *p*-methylphenoxyl radical by Un<sup>7</sup> also observed an increase in the splitting ( $\Delta E^*$ ) between the oxygen lone pair nonbonding orbital and the half filled  $\pi$  orbital upon hydrogen bonding due to the stabilization of the non-bonding orbital. It is clear, therefore, that both the MO energies and the oxygen spin density contribute to the electron *g* value shifts observed for hydrogen-bonded tyrosyl radicals.

While the variation in spin densities with hydrogen bond length that we observe in our theoretical calculations is in qualitative agreement with other theoretical studies, our calculations are not, in general, in good agreement with the spin densities estimated for different hydrogen-bonded tyrosyl radicals from experimental ENDOR hyperfine data with the McConnell relations (eqs 5 and 6). The isotropic hyperfine coupling ( $A_{\text{iso}}$ ) for a proton ( $H_i$ ) can be related to its adjacent carbon ( $C_i$ ) spin density by the McConnell constant  $Q_H$ , while the isotropic and *z* principal component ( $A_z$ ) of the <sup>17</sup>O hyperfine coupling can be related to the oxygen spin density by the empirical constants  $Q_O$  and  $B_O$ , respectively.

$$A_{\text{iso}}(^1H_i) = Q_H \rho_{C_i} \quad (5)$$

$$A_{\text{iso}}(^{17}O) = Q_O \rho_O \quad \text{and} \quad A_z(^{17}O) = 2B_O \rho_O \quad (6)$$

In the EPR study by Fasanella and Gordy of  $\gamma$ -irradiated Tyr•HCl crystals<sup>51</sup> the spectra were attributed to a neutral radical which was observed, in a neutron diffraction study, to have a 1.6 Å hydrogen bond.<sup>45</sup> In addition, theoretical MNDO calculations of the electron *g* values for Tyr•HCl crystals by

Sun *et al.* find the best fit to the experimental *g* values for a hydrogen bond distance of 1.59 Å.<sup>7</sup> From the carbon spin densities estimated by Fasanella and Gordy, an oxygen spin density of  $\rho_O = 0.30$  is obtained.<sup>9</sup> This estimated oxygen spin density is in good agreement with the spin density we calculate for the *p*-methylphenoxyl radical with a 1.6 Å hydrogen bond. However, such good agreement between our calculations and ENDOR-derived spin densities is not observed for *Synechocystis* PS II, spinach PS II, and *E. coli* RNR. Force *et al.* estimated a tyrosyl hydrogen bond distance of 1.87 Å for *Synechocystis* PS II.<sup>6</sup> Estimates of 1.85 and 1.7 Å for the hydrogen bond distance in *Synechocystis* were also made by Tang *et al.*<sup>52</sup> and Un *et al.*<sup>7</sup>, respectively. The ENDOR-estimated spin density of  $\rho_O = 0.26$  for *Synechocystis* PS II<sup>9</sup> is less than the  $\rho_O = 0.31$  predicted for a 1.7–1.8 Å hydrogen bond by our density functional calculations. A tyrosyl hydrogen bond distance of 1.67 Å was estimated for spinach PS II by Force *et al.*<sup>6</sup> Again, the ENDOR-estimated spin density of  $\rho_O = 0.22^{37} is considerably less than that predicted by our calculations for a 1.6–1.7 Å hydrogen bond (0.30–0.31). The oxygen spin density of  $\rho_O = 0.29$  in the non-hydrogen bonded tyrosyl radical of *E. coli* RNR, estimated by Hoganson *et al.* from measured <sup>17</sup>O ENDOR hyperfine couplings and the McConnell relation (eq 6),<sup>53</sup> is 10% less than that predicted by our calculations for a non-hydrogen bonded radical.$

The spin density distributions derived from the use of ENDOR data in conjunction with the McConnell relation are also inconsistent with experimentally measured *g* values. As has been discussed, the *g*<sub>1</sub> values measured for Tyr•HCl, mouse RNR, and *E. coli* RNR accurately reflect their respective hydrogen-bonding status (see Table 2). However, examination of Table 4 reveals no consistent trend for McConnell relation derived oxygen spin density as a function of hydrogen bonding. In particular, the oxygen spin densities for the hydrogen-bonded tyrosyl radicals of Tyr•HCl (0.34) and mouse RNR (0.30) are both greater than the spin density for *E. coli* RNR (0.29).

The discrepancy between the density functional calculated and the ENDOR-estimated spin densities remains under investigation. However, a possible source of the disagreement may be due to the empirical constant *Q* used in the McConnell relations.<sup>42,43,50</sup> The reported *E. coli* RNR oxygen spin density (Table 4) is estimated directly from <sup>17</sup>O hyperfine data using eq 6.<sup>53</sup> The McConnell constant used is that determined for peroxide systems,  $Q(^{17}O) = -40.0$  G, by Sevilla *et al.*<sup>54</sup> and Broze *et al.*<sup>55</sup> Recent density functional calculations by Himo *et al.* suggest that a value of  $Q(^{17}O) = -20.5$  G is more appropriate for tyrosyl radicals and that great care must be taken in the choice of the empirical parameters used in the McConnell relations.<sup>50</sup> Himo *et al.* performed density functional calculations of the <sup>17</sup>O hyperfine couplings as well as the electron spin

density distribution in model *p*-ethylphenoxyl radicals. The calculated  $^{17}\text{O}$  hyperfine couplings were found to be in good agreement with experimental ENDOR data yet the computed oxygen spin densities were significantly greater than those estimated from the ENDOR data using the McConnell eq. Most of the oxygen spin densities tabulated in Table 4 have been determined indirectly from estimated tyrosyl ring carbon densities (see eq 5) where the spin density not accounted for by ring carbons is assumed to reside on the oxygen. A McConnell constant of  $Q(^1\text{H}) = -24.9$  G was used to relate the experimental *E. coli* RNR proton hyperfine couplings to the adjacent ring carbon spin densities.<sup>53</sup> The density functional study of Himo *et al.* again found good agreement with the ENDOR-measured proton hyperfine couplings; however, their calculated value of  $Q(^1\text{H}) = -13$  G for  $\text{H}_2/\text{H}_6$  is half the value used in the ENDOR study.<sup>50</sup> Errors in calculating the spin densities from the McConnell eq can also arise if spin densities from neighboring atomic centers and hydrogen-bonding effects are not considered.<sup>42,43</sup> It is anticipated, however, that continued refinement of the density functional calculations and the McConnell  $Q$  values will bring the theoretically and experimentally derived spin densities into agreement.

## Summary

High-frequency EPR spectroscopy allows the resolution of the small *g*-anisotropy typical of organic  $\pi$  radicals, providing insight into their electronic and molecular structure. Both the *g* anisotropy and electron–nuclear hyperfine couplings are resolved in the 139.5 GHz saturated dispersion EPR spectrum of the  $\text{Y}_\text{D}$  tyrosyl radical in photosystem II. The experimental spectrum is only faithfully replicated in simulations which account for the saturated dispersion line shape. The hyperfine couplings determined from the spectral simulations are in good agreement with those obtained from X-band  $^1\text{H}$  ESE–ENDOR spectra of Mn-depleted samples.  $\Delta g_1$  has previously been demonstrated to be a sensitive monitor of hydrogen bonding to the phenyl oxygen of tyrosyl radicals; increased hydrogen bonding is associated with decreased shifts in  $g_1$  from the free electron *g* value compared to non-hydrogen bonded radicals. Density functional calculations of the model *p*-methylphenoxyl radical indicate that hydrogen bonding both reduces the electron spin density on oxygen, by as much as 30% for a 1.1 Å hydrogen bond, and increases the orbital splitting between the singly occupied molecular orbital and nearest excited state SOMOs. Both these factors contribute to the reduced *g*-shifts observed for hydrogen-bonded tyrosyl radicals.

**Acknowledgment.** We gratefully acknowledge the support of the National Institutes of Health (GM-38352, RR-00995, and GM-48242) and the National Science Foundation (MCB-95-13648).

## References and Notes

- (1) Diner, B. A.; Babcock, G. T. In *Oxygenic Photosynthesis*; Ort, D. R., Yocum, C. F., Ed.; Kluwer Academic Publishers: Dordrecht, The Netherlands, 1996; pp 213–247.
- (2) Gilchrist, M. L.; Ball, J. A.; Randall, D. W.; Britt, R. D. *Proc. Natl. Acad. Sci. U.S.A.* **1995**, *92*, 9545–9549.
- (3) Hoganson, C. W.; Lydakis-Simantiris, N.; Tang, X.-S.; Tommos, C.; Warncke, K.; Babcock, G. T.; Diner, B. A.; McCracken, J.; Styring, S. *Photosynth. Res.* **1995**, *46*, 177–184.
- (4) Tang, X.-S.; Chisholm, D. A.; Dismukes, G. C.; Brudvig, G. W.; Diner, B. A. *Biochemistry* **1993**, *32*, 13742–13748.
- (5) Kirilovsky, D. L.; Boussac, A. G. P.; van Mieghem, F. J. E.; Ducruet, J.-M. R. C.; Setif, P. R.; Yu, J.; Vermaas, W. F. J.; Rutherford, A. W. *Biochemistry* **1992**, *31*, 2099–2107.
- (6) Force, D. A.; Randall, D. W.; Britt, R. D.; Tang, X.-S.; Diner, B. A. *J. Am. Chem. Soc.* **1995**, *117*, 12643–12644.
- (7) Un, S.; Atta, M.; Fontecave, M.; Rutherford, A. W. *J. Am. Chem. Soc.* **1995**, *117*, 10713–10719.
- (8) Campbell, K.; Peloquin, J.; Diner, B. A.; Tang, X.-S.; Britt, R. D. *J. Am. Chem. Soc.*, submitted for publication.
- (9) Tommos, C.; Tang, X.-S.; Warncke, K.; Hoganson, C. W.; Styring, S.; McCracken, J.; Diner, B. A.; Babcock, G. T. *J. Am. Chem. Soc.* **1995**, *117*, 10325–10335.
- (10) Diner, B. A.; Tang, X.-S.; Zheng, M.; Dismukes, G. C.; Force, D. A.; Randall, D. W.; Britt, R. D. In *Photosynthesis: From Light to Biosphere*; Mathis, P., Ed.; Kluwer Academic Publishers: Amsterdam, 1995; Vol. II, pp 229–234.
- (11) Dixon, W. T.; Murphy, D. J. *Chem. Soc., Faraday Trans.* **1976**, *72*, 1221–1230.
- (12) Lee, J. Y.; Box, H. C. *J. Chem. Phys.* **1973**, *59*, 2509–2512.
- (13) Burghaus, O.; Plato, M.; Rohrer, M.; Mobius, K.; MacMillan, F.; Lubitz, W. *J. Phys. Chem.* **1993**, *97*, 7639–7647.
- (14) Un, S.; Tang, X.-S.; Diner, B. A. *Biochemistry* **1996**, *35*, 679–684.
- (15) Gerfen, G. J.; Bellew, B. F.; Un, S.; Bollinger, J. M.; Stubbe, J.; Griffin, R. G.; Singel, D. J. *J. Am. Chem. Soc.* **1993**, *115*, 6420–6421.
- (16) Schmidt, P. P.; Andersson, K. K.; Barra, A.-L.; Thelander, L.; Gräslund, A. *J. Biol. Chem.* **1996**, *271*, 23615–23618.
- (17) Un, S.; Brunel, L.-C.; Brill, T. M.; Zimmermann, J.-L.; Rutherford, A. W. *Proc. Natl. Acad. Sci. U.S.A.* **1994**, *91*, 5262–5266.
- (18) Stone, A. J. *Mol. Phys.* **1963**, *6*, 509–515.
- (19) Qin, Y.; Wheeler, R. A. *J. Chem. Phys.* **1995**, *102*, 1689–1698.
- (20) Berthold, D. A.; Babcock, G. T.; Yocum, C. F. *FEBS Lett.* **1981**, *134*, 231–234.
- (21) Ford, R. C.; Evans, M. C. W. *FEBS Lett.* **1983**, 159–164.
- (22) Arnon, D. I. *Plant Physiol.* **1949**, *24*, 1–14.
- (23) Becerra, L. R.; Gerfen, G. J.; Bellew, B. F.; Bryant, J. A.; Hall, D. A.; Inati, S. J.; Weber, R. T.; Un, S.; Prisner, T. F.; McDermott, A. E.; Fishbein, K. W.; Kreischer, K. E.; Temkin, R. J.; Singel, D. J.; Griffin, R. G. *J. Magn. Reson.* **1995**, *117*, 28–40.
- (24) van der Donk, W. A.; Stubbe, J.; Gerfen, G. J.; Bellew, B. F.; Griffin, R. G. *J. Am. Chem. Soc.* **1995**, *117*, 8908–8916.
- (25) Hyde, J. S.; Jesmanowicz, A.; Ratke, J. J.; Antholine, W. E. *J. Magn. Reson.* **1992**, *96*, 1–13.
- (26) Frisch, M. J.; Trucks, G. W.; Schlegel, H. B.; Gill, P. M. W.; Johnson, B. G.; Robb, M. A.; Cheeseman, J. R.; Keith, T.; Petersson, G. A.; Montgomery, J. A.; Raghavachari, K.; Al-Laham, M. A.; Zakrzewski, V. G.; Ortiz, J. V.; Foresman, J. B.; Peng, C. Y.; Ayala, P. Y.; Chen, W.; Wong, M. W.; Andres, J. L.; Replogle, E. S.; Gomperts, R.; Martin, R. L.; Fox, D. J.; Binkley, J. S.; Defrees, D. J.; Baker, J.; Stewart, J. P.; Head-Gordon, M.; Gonzalez, C.; Pople, J. A. *Gaussian94* Revision D.3; Gaussian, Inc.: Pittsburgh, PA, 1994.
- (27) Slater, J. C. *Quantum Theory of Molecules and Solids*; McGraw Hill: New York, 1974; Vol. 4.
- (28) Vosko, S. H.; Wilk, L.; Nusair, M. *Can. J. Phys.* **1980**, *58*, 1200–1211.
- (29) Hehre, W. J.; Radom, L.; Schleyer, P. v. R.; Pople, J. A. *Ab Initio Molecular Orbital Theory*; Wiley: New York, 1986.
- (30) Davidson, E. R.; Feller, D. *Chem. Rev.* **1986**, *86*, 681–696.
- (31) Walden, S. E.; Wheeler, R. A. *J. Phys. Chem.* **1996**, *100*, 1530–1535.
- (32) Qin, Y.; Wheeler, R. A. *J. Am. Chem. Soc.* **1995**, *117*, 6083–6092.
- (33) Qin, Y.; Wheeler, R. A. *J. Phys. Chem.* **1996**, *100*, 10554–10563.
- (34) Chipman, D. M.; Liu, R.; Zhou, X.; Pulay, P. *J. Chem. Phys.* **1994**, *100*, 5023–5035.
- (35) Liu, R.; Zhou, X. *J. Phys. Chem.* **1993**, *97*, 9613–9617.
- (36) Warncke, K.; Babcock, G. T.; McCracken, J. *J. Am. Chem. Soc.* **1994**, *116*, 7332–7340.
- (37) Rigby, S. E. J.; Nugent, J. H. A.; O'Malley, P. J. *Biochemistry* **1994**, *33*, 1734–1742.
- (38) Poole, C. P. *Electron Spin Resonance: A Comprehensive Treatise on Experimental Techniques*, 2nd ed.; John Wiley & Sons: New York, 1983; pp 577–600.
- (39) Portis, A. M. *Phys. Rev.* **1953**, *91*, 1071–1078.
- (40) Portis, A. M. Magnetic Resonance in Systems with Spectral Distributions. Technical Note 1; Sarah Mellon Radiation Laboratory, University of Pittsburgh, 1955.
- (41) Ammerlaan, C. A. J.; van der Weil, A. *J. Magn. Reson.* **1976**, *21*, 387–396.
- (42) Felix, C. C.; Prabhananda, B. S. *J. Chem. Phys.* **1984**, *80*, 3078–3081.
- (43) Prabhananda, B. S. *J. Chem. Phys.* **1983**, *79*, 5752–5757.
- (44) Bowman, M. K.; Thurnauer, M. C.; Norris, J. R.; Dikanov, S. A.; Gulín, V. I.; Tryshkin, A. M.; Samoilova, R. I.; Tsvetkov, Y. D. *Appl. Magn. Reson.* **1992**, *3*, 353–368.
- (45) Frey, M. N.; Koetzle, T. F.; Lehmann, M. S.; Hamilton, W. C. *J. Chem. Phys.* **1973**, *58*, 2547–2556.



- (46) Bender, C. J.; Sahlin, M.; Babcock, G. T.; Barry, B. A.; Chandrasekar, T. K.; Salowe, S. P.; Stubbe, J.; Lindström, B.; Ehrenberg, A.; Sjöberg, B.-M. *J. Am. Chem. Soc.* **1989**, *111*, 8076–8083.
- (47) Stone, A. J. *Proc. R. Soc. A* **1963**, *271*, 424–434.
- (48) Stone, A. J. *Mol. Phys.* **1964**, *7*, 311–316.
- (49) Feher, G.; Isaacson, R. A.; Okamura, M. Y.; Lubitz, W. In *Springer Series in Chemical Physics*; Michel-Beyerle, M. E., Ed.; Springer-Verlag: Berlin, 1985; pp 174–189.
- (50) Himo, F.; Gräslund, A.; Eriksson, L. A. *Biophys. J.* **1997**, *72*, 1556–1567.
- (51) Fasanella, E. L.; Gordy, W. *Proc. Natl. Acad. Sci. U.S.A.* **1969**, *62*, 299–304.
- (52) Tang, X.-S.; Zheng, M.; Chisholm, D. A.; Dismukes, G. C.; Diner, B. A. *Biochemistry* **1996**, *35*, 1475–1484.
- (53) Hoganson, C. W.; Sahlin, M.; Sjöberg, B.-M.; Babcock, G. T. *J. Am. Chem. Soc.* **1996**, *118*, 4672–4679.
- (54) Sevilla, M. D.; Becker, D.; Yan, M. *J. Chem. Soc., Faraday Trans.* **1990**, *86*, 3279–3286.
- (55) Broze, M.; Luz, Z.; Silver, B. J. *J. Chem. Phys.* **1967**, *46*, 4891–4902.
- (56) Allard, P.; Barra, A. L.; Andersson, K. K.; Schmidt, P. P.; Atta, M.; Gräslund, A. *J. Am. Chem. Soc.* **1996**, *118*, 895–896.
- (57) Warncke, K.; McCracken, J. *J. Chem. Phys.* **1995**, *103*, 6829–6840.
- (58) Hoganson, C. W.; Babcock, G. T. *Biochemistry* **1992**, *31*, 11874–11880.